AGU PUBLICATIONS

Geophysical Research Letters

RESEARCH LETTER
10.1002/2017GL072874

Key Points:
- A high-accuracy global digital elevation model (DEM) was developed by removing multiple height error components from existing DEMs
- Landscape representation was improved, especially in flat regions where height error magnitude was larger than actual topography variation
- The improved-terrain DEM is helpful for any geoscience applications which are terrain dependent, such as flood inundation modelling

Supporting Information:
- Supporting Information S1

Correspondence to:
D. Yamazaki,
yamadai@rainbow.iis.u-tokyo.ac.jp

Citation:
Yamazaki, D., D. Ikeshima, R. Tawatari, T. Yamaguchi, F. O'Loughlin, J. C. Neal, C. C. Sampson, S. Kanae, and P. D. Bates (2017), A high-accuracy map of global terrain elevations, *Geophys. Res. Lett.*, *44*, 5844–5853, doi:10.1002/2017GL072874.

Received 30 JAN 2017
Accepted 19 MAY 2017
Accepted article online 31 May 2017
Published online 14 JUN 2017

A high-accuracy map of global terrain elevations

Dai Yamazaki[1,2], Daiki Ikeshima[3], Ryunosuke Tawatari[3], Tomohiro Yamaguchi[4], Fiachra O'Loughlin[5], Jeffery C. Neal[6], Christopher C. Sampson[7], Shinjiro Kanae[3], and Paul D. Bates[6]

[1]Department of Integrated Climate Change Projection Research, Japan Agency for Marine-Earth Science and Technology, Yokohama, Japan, [2]Institute of Industrial Sciences, University of Tokyo, Tokyo, Japan, [3]Department of Civil and Environmental Engineering, Tokyo Institute of Technology, Tokyo, Japan, [4]Institute of Space and Astronautical Science, Japan Aerospace Exploration Agency, Sagamihara, Japan, [5]UCD School of Civil Engineering, University College Dublin, Dublin, Ireland, [6]School of Geographical Sciences, University of Bristol, Bristol, UK, [7]SSBN, Bristol, UK

Abstract Spaceborne digital elevation models (DEMs) are a fundamental input for many geoscience studies, but they still include nonnegligible height errors. Here we introduce a high-accuracy global DEM at 3″ resolution (~90 m at the equator) by eliminating major error components from existing DEMs. We separated absolute bias, stripe noise, speckle noise, and tree height bias using multiple satellite data sets and filtering techniques. After the error removal, land areas mapped with ±2 m or better vertical accuracy were increased from 39% to 58%. Significant improvements were found in flat regions where height errors larger than topography variability, and landscapes such as river networks and hill-valley structures, became clearly represented. We found the topography slope of previous DEMs was largely distorted in most of world major floodplains (e.g., Ganges, Nile, Niger, and Mekong) and swamp forests (e.g., Amazon, Congo, and Vasyugan). The newly developed DEM will enhance many geoscience applications which are terrain dependent.

Plain Language Summary Terrain elevation maps are fundamental input data for many geoscience studies. While very precise Digital Elevation Models (DEMs) based on airborne measurements are available in developed regions of the world, most areas of the globe rely on spaceborne DEMs which still include non-negligible height errors for geoscience applications. Here we developed a new high accuracy map of global terrain elevations at 3" resolution (~90m at the equator) by eliminating multiple error components from existing spaceborne DEMs. The height errors included in the original DEMs were separated from actual topography signals and removed using a combination of multiple satellite datasets and filtering techniques. After error removal, global land areas mapped with ±2m or better accuracy increased from 39% to 58%. Significant improvements were found, especially in flat regions such as river floodplains. Here detected height errors were larger than actual topography variability, and following error removal landscapes features such as river networks and hill-valley structures at last became clearly represented. The developed high accuracy topography map will expand the possibility of geoscience applications that require high accuracy elevation data such as terrain landscape analysis, flood inundation modelling, soil erosion analysis, and wetland carbon cycle studies.

1. Introduction

Precise representation of global terrain is a fundamental goal of geodetic survey, and essential for studies including topography classification for earthquake motion assessment [*Hough et al*., 2010], flood inundation modeling [*Yamazaki et al*., 2014; *Sampson et al*., 2016], global wetland carbon dynamics [*Laudon et al*., 2011], soil erosion and sediment yield prediction [*de Vente et al*., 2013], and water mapping by remote sensing [*Pekel et al*., 2016]. While high-accuracy airborne digital elevation models (DEMs) are available in developed countries, many regions of the world still rely on spaceborne DEMs. Accuracy of terrain elevation mapping has improved in recent years as a result of advances in remote sensing techniques, and this has facilitated progress in all the above research areas. For example, the Shuttle Radar Topography Mission (SRTM) measured land elevations using radar interferometry and provides a near-global DEM at 1″ and 3″ resolution [*Farr et al*., 2007]. More recently, higher spatial resolution global DEMs, such as ASTER GDEM (Advanced Spaceborne Thermal Emission and Reflection Radiometer-Global DEM) [*Tachikawa et al*., 2011] and AW3D-DEM (ALOS: Advanced Land Observing Satellite, World 3D-DEM) [*Tadono et al*., 2015], have been developed using stereo viewing of optical satellite images.

However, spaceborne DEMs contain various observational errors, which are nonnegligible for geoscience applications. Random components of height errors can be classified by their spatial scale into short-wavelength (a few pixels) speckle noise, medium-wavelength (500 m ~ 50 km) stripe noise, and long-wavelength (>20 km) absolute biases [*Rodriguez et al*., 2006; *Dowling et al*., 2011]. Spaceborne DEMs are also affected by systematic positive biases due to tree canopies in forested areas [*O'Loughlin et al*., 2016a], even though a "bare-earth DEM" which represents the elevation of the ground below the tree canopy is essential for many applications. Each height error component has a magnitude as large as 10 m, and such errors are significantly problematic for many geoscience applications. For example, the amplitude of the planet's largest flood wave (the Amazon) is only 12 m [*Baugh et al*., 2013; *Rudorff et al*., 2014], and most flood waves have amplitudes of just a few meters [*Yamazaki et al*., 2014; *Sampson et al*., 2015]. Storm surges and Tsunami wave heights are generally <10 m [*Tang et al*., 2009], and both landslides and soil erosion are strongly conditioned by terrain slope [*Hough et al*., 2010; *de Vente et al*., 2013]. Noise and bias obscure landscape features such as river networks and hill-valley topographies that are critical to vertical meteorological fluxes [*Maxwell and Condon*, 2016], lateral hydrological and biogeochemical fluxes [*Baugh et al*., 2013; *Rudorff et al*., 2014], and ecological patterns [*Fluet-Chouinard et al*., 2015].

Methods for removing the speckle noise [*Gallant*, 2011], stripe noise [*Tarekegn and Sayama*, 2013; *Gallant and Read*, 2009], absolute bias [*Rudorff et al*., 2014; *Berry et al*., 2010], and tree height bias [*O'Loughlin et al*., 2016a; *Baugh et al*., 2013] from spaceborne DEMs have been developed by utilizing other satellite data sets and filtering techniques. However, most previous methods were only applied to limited regions of the globe because some manual processes were unavoidable [*Baugh et al*., 2013; *Rudorff et al*., 2014; *Gallant*, 2011; *Tarekegn and Sayama*, 2013; *Gallant and Read*, 2009]. Otherwise, previous global-scale correction methods have only treated a single error component [*O'Loughlin et al*., 2016a; *Berry et al*., 2010], which is not sufficient to give a generally applicable solution to the problem. Accurate estimation of error magnitude is impossible if only one error component is considered because different error components could cancel each other out. There is thus a need to develop a globally consistent error removal method that treats all major components of DEM errors. In this paper, we developed a very accurate mapping of global terrain elevations achieved by correcting all major error components in spaceborne DEMs.

2. Data and Method

2.1. Input Data Sources

The SRTM3 DEM (below N60°) [*Farr et al*., 2007] and the AW3D-30 m DEM (above N60°) [*Tadono et al*., 2015] were used as the baseline DEMs. The unobserved areas in both DEMs were filled with the Viewfinder Panoramas DEM (VFP-DEM, supporting information Figure S1a).

The SRTM3 DEM was generated by C-band radar interferometry on board the space shuttle during February 2000. It covered lands between N60° and S56° at 3″ resolution, but there are some observation gaps in high-relief mountains and over water bodies. A gap filled version developed by CGIAR-Consortium for Spatial Information was available [*Jarvis et al*., 2008]; however, we did not use this because of some critical errors in the void filling procedures (supporting information Figure S1b).

The AW3D DEM was generated by the "Panchromatic Remote-sensing Instrument for Stereo Mapping (PRISM)" on the "Advanced Land Observing Satellite (ALOS)" which operated from January 2006 to April 2011. The land elevations were acquired by along-track stereo viewing using the three-directional PRISM sensor. The original commercial version has a 5 m spatial resolution, while we used the freely available 1″ version (AW3D-30 m DEM median product) and converted the resolution to 3″ by taking 3 × 3 pixel means. The AW3D DEM covers areas between S82° and N82°, but many observation gaps occur in (1) the tropics and high latitudes because of cloud cover and (2) over water due to low correlation problems.

The VFP-DEM (available at http://www.viewfinderpanoramas.org/dem3.html) was used for filling observation gaps in the SRTM3 and AW3D DEMs. The VFP-DEM was developed by carefully filling the SRTM unobserved areas using other data sets such as digitized paper topography maps, Canadian Geobase DEM [*Johnson and Singh*, 2003] and the U.S. National Elevation Data [*Gesch et al*., 2014]. It covers the entire globe at 3″ resolution. Though the data source, quality and effective resolution of the VFP-DEM are not consistent across the globe, its accuracy is better than other low-resolution DEMs above N60° (such as GMTED2010 [*Danielson and Gesch*, 2011]

and supporting information Figure S1c). We manually corrected some obviously strange elevations of the VFP-DEM before merging with the SRTM3 and AW3D DEMs. Note that we did not use the ASTER GDEM [*Tachikawa et al*., 2011], because its height errors are reported to be larger than the SRTM and AW3D DEMs [*Hirt et al*., 2010] (supporting information Figure S1d).

The ICESat (Ice, Cloud, and land Elevation Satellite) laser altimetry [*Harding and Carabajal*, 2005] was used as the reference ground elevation for estimating biases in the DEMs. We also used a global tree density map [*Hansen et al.,* 2013] and tree height map [*Simard et al*., 2011] to estimate errors due to forest canopy. Detailed descriptions of the ICESat data and tree density/height maps are provided in supporting information Text S1 and Figure S2.

2.2. Error Removal Procedures

The major vertical height errors of spaceborne DEMs can be classified into four components: speckle noise, stripe noise, absolute bias, and tree height bias. Speckle noise is a random error with very short wavelength of a few pixels, mainly caused by variability of surface reflectance over flat terrain [*Rodriguez et al*., 2006; *Takaku et al*., 2016]. Stripe noise is a regular height undulation with a wavelength of 500 m to 100 km [*Tarekegn and Sayama*, 2013; *Gallant and Read*, 2009; *Crippen et al*., 2016]. The stripe noise of the SRTM DEM was mainly a result of residual motion errors of the interferometry mast [*Rodriguez et al*., 2006], while that of the AW3D DEM was caused by the artificial tilt of elevations within a swath (positive bias in west side of each swath, and negative in east side, supporting information Figure S1d). The absolute bias can be recognized as a shift in the average elevation over a large domain (typically $>$20 km scale). It is difficult to determine the absolute elevations both by radar interferometry and stereo viewing of optical images, and both method needs ground control points for reference elevations [*Takaku et al*., 2015; *Crippen et al*., 2016]. The absolute bias therefore tends to be large where high-quality ground control points are not available. The tree height bias was caused because both radar interferometry and stereo viewing of optical images cannot measure terrain elevations beneath forest canopies [*O'Loughlin et al*., 2016a; *Carabajal and Harding*, 2006].

We developed a four-step method for separating and removing the four major error components in spaceborne DEMs (Figure 1). First, the stripe noise was removed by detecting unrealistic regular terrain undulations using a two-dimensional Fourier transform filter. Second, the absolute bias was detected by calculating the difference between the DEM and the ICESat centroid elevations. Third, the tree height bias was estimated as a function of tree density and tree height, which was constructed by comparing the DEM, global forest data sets, and ICESat lowest elevations. Finally, the speckle noise was removed by applying an adaptive smoothing filter that statistically separates speckle noise and topography signals [*Gallant*, 2011]. While the adaptive smoothing filter for speckle noise removal was coded following its description paper [*Gallant*, 2011], the algorithms to remove the other error components were developed for this study.

The order in which the four error removal steps were performed was decided for the following reasons: (1) the stripe noise could affect the estimation of absolute bias; thus, it should be removed first; (2) in order to estimate the tree height bias by referencing the ICESat lowest elevations, absolute biases have to be removed beforehand; and (3) tree height bias in patchy forest areas could be removed altogether along with the speckle noise by a smoothing filter; thus, the tree height bias should be removed before smoothing the speckle noise. Following the above logic, the error detection and removal was applied in the following order: stripe noise, absolute bias, tree height bias, and, finally, speckle noise. The processing chain used is summarized in Figure 1a.

Hereafter the newly developed terrain elevation map is referred to as the "new DEM." A detailed description of the error removal method is given in supporting information Text S2 and Figures S3–S7.

3. Results and Validation

3.1. Spatial Pattern of Detected Errors

The spatial patterns of the detected errors were different for different error components and different DEM sources (Figure 1). Stripe noise with ~15 km wavelength and ~10 m maximum amplitude along the shuttle orbit direction was dominant in the SRTM domain (below N60°). In the AW3D domain, stripe noise with ~35 km wavelength due to the elevation tilt within each observation swath (supporting information Figure S1d) was found in the across-track direction. Speckle noise was most easily detected in flat areas where it can be statistically separated from the topography signal, and large magnitude speckle noise (~10 m)

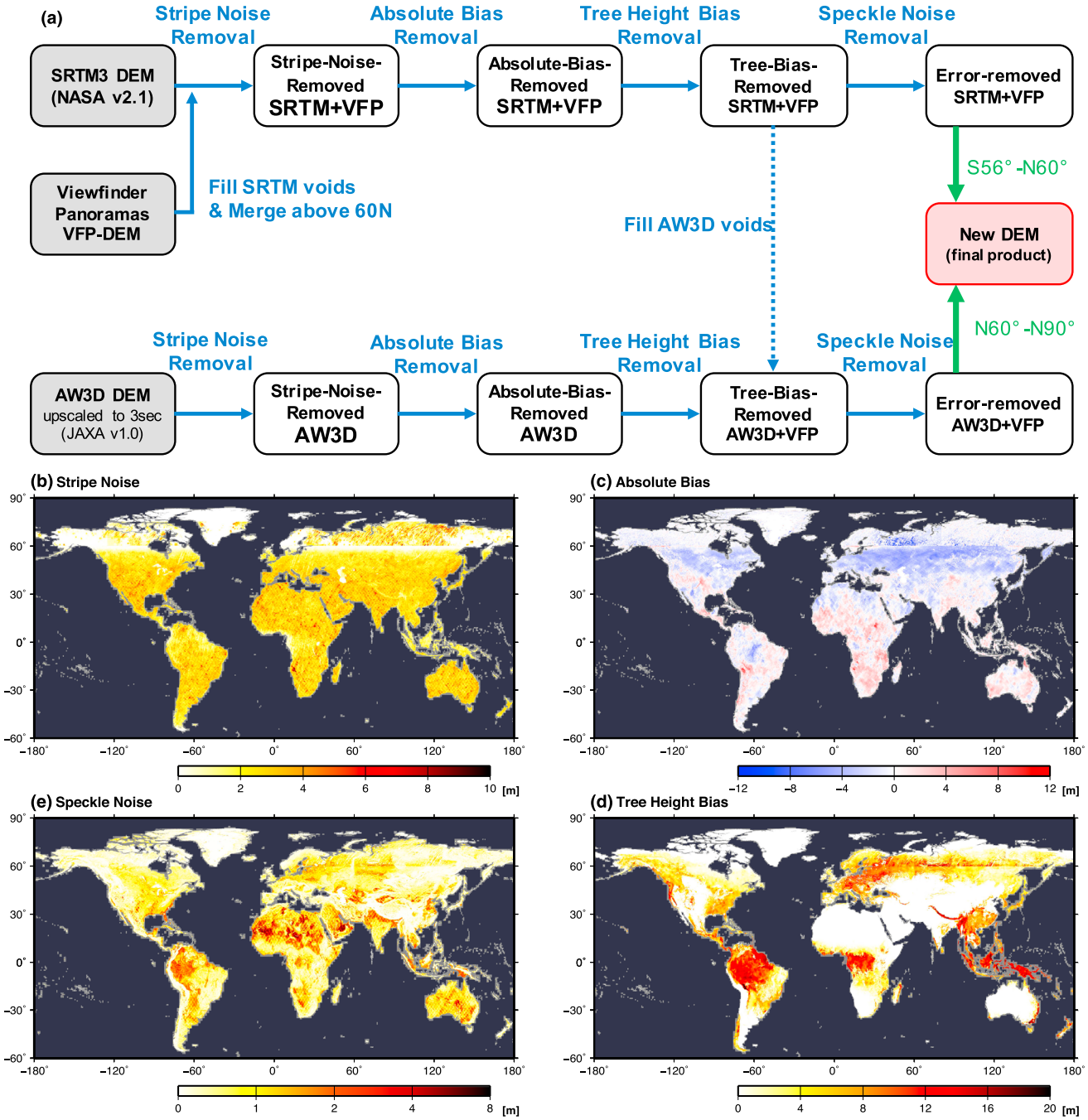

Figure 1. Procedures of error removal. Schematic diagram. Spatial pattern of detected errors of error removal procedures. The 90th percentile value in each 0.1° tile is shown for (b) stripe noise, (c) absolute bias, (d) tree height bias, and (e) speckle noise. The absolute magnitudes are shown for stripe and speckle noise for clear visualization purpose. The discontinuity around N60° corresponds to the boundary of the SRTM and AW3D DEMs.

appears to occur mainly in deserts where surface reflectance variability is large [*Rodriguez et al.*, 2006]. The spatial patterns of stripe and speckle noise also correspond to satellite orbit tracks because the error amplitude was reduced in the processing of the original DEMs by overlaying multiple observations [*Rodriguez et al.*, 2006].

Absolute biases caused by long-wavelength random residual satellite motion errors [*Rodriguez et al.*, 2006] were found in the SRTM domain, but their spatial pattern was uneven because multiple observations with different absolute biases were overlaid when the DEM was created. In general, absolute bias was negative

(up to −8 m) between N40° and N60°, while positive bias (up to 10 m) was found in many parts of Africa, Australia, and South America (except the Amazon). The absolute bias of the AW3D DEM was in general smaller because the absolute heights of the AW3D were originally referenced to ICESat centroid elevations which provides better ground control points [*Takaku et al*., 2015]. However, negative absolute biases up to −15 m were found, probably because the AW3D DEM was wrongly referenced to tree canopy height [*Takaku et al*., 2015]. The tree height bias followed the spatial distribution of forested areas, with a maximum amplitude of ~20 m in the tropics and Western Siberia. The tree height bias was larger for AW3D than SRTM around their boundary along N60° due to the difference in sensor-dependent height measurement in forested regions (supporting information Figure S4). The detected error patterns also suggested the importance of considering multiple error components for DEM improvement. For example, Western Siberia was affected by both negative absolute biases and positive tree height biases. Given that the detailed spatial distributions of these two errors were different, reasonable error removal could not be achieved if only one error component was treated. The occurrence of canceling terms could occur between any two of the four error terms and might occur in heterogeneous spatial patterns across the globe.

3.2. Accuracy Assessment

The accuracy of the new DEM was assessed using ICESat lowest elevations which represent terrain elevations both in forested and nonforested areas [*Harding and Carabajal*, 2005]. First, large-scale errors were investigated by calculating mean errors between the DEM and ICESat elevations within 0.1° tiles (Figure 2a). The original DEM had both positive and negative errors mainly due to the absolute bias and tree height bias, but most negative errors disappeared after the removal of stripe noise and absolute bias. The positive biases in forested areas were largely reduced in the new DEM after the removal of all major error components. Positive biases remained in mountainous regions of the new DEM because of the large subpixel topography variability resulting from steep slopes. While ICESat lowest elevations correspond to the lowest point within this satellite's ~70 m footprint, DEM elevations represent the mean elevation within each 3″ resolution (~90 m at the equator) pixel, resulting in positive biases in mountainous regions with large subpixel variability.

The pixel-scale errors were also largely reduced in the new DEM (Figure 2b). 58% of land pixels were mapped with better than 2 m height accuracy in the new DEM, improved from 39% in the original DEM. The 90th percentile error was also reduced from ±14 m to ±12 m. If pixels with topography slope $>$ 10% were excluded, 72% areas were mapped with better than 2 m accuracy and the 90th percentile error of the new DEM was smaller than ±5 m. This suggests most residual errors in the new DEM correspond to subpixel variability in mountainous areas. The 90th percentile error in flat forested areas (topography slope $<$ 10% and tree density $>$ 30%) was improved significantly from 17 m to 9 m.

The above accuracy could be overestimated because the ICESat elevations were also used for removing absolute bias and tree height bias. Therefore, we performed a cross validation by dividing the ICESat observations into calibration and validation data. We divided the land surface into 1/6° tiles, and ICESat observations located within the lower right of a 2 × 2 tile window were excluded from use in the error removal steps and instead were employed as validation data. The results of the cross-validation experiment are summarized in histograms (supporting information Figure S8). The calibration tiles and validation tiles have similar histograms in the original DEMs, and the pattern of histograms was also similar in the new DEM after the error removal, even though ICESat observations were not used in validation tiles. The accuracy was slightly lower in validation tiles (56% of all land pixels have height errors $<$2 m) compared to the calibration grid (58%). Given that the spatial scales of the absolute bias and tree height bias were relatively large, the biases in validation tiles could be reasonably estimated by interpolating ICESat observations in nearby calibration tiles. This result suggests that the accuracy of the new DEM in pixels without ICESat observations is almost the same as the accuracy in pixels where ICESat observations are present.

The accuracy of the new DEM was also validated against a local high-quality DEM. We used the UK airborne lidar DEM (available at https://data.gov.uk/dataset/lidar-composite-dsm-1m1) and performed validation in the Fens region of eastern England (N52.6°–N52.8°, W0.3°–E0.3°, supporting information Figure S9). This is a bare-earth DEM with horizontal resolution of 1 m and vertical accuracy $<$10 cm root-mean-square error produced by the UK Environment Agency. We converted the reference geoid of the UK lidar DEM to EGM96 and resampled it at 3″ resolution in order to make an accurate comparison to the global DEMs. While the original SRTM DEM was affected by a negative absolute bias (~1 m) and also by significant stripe noise in this region,

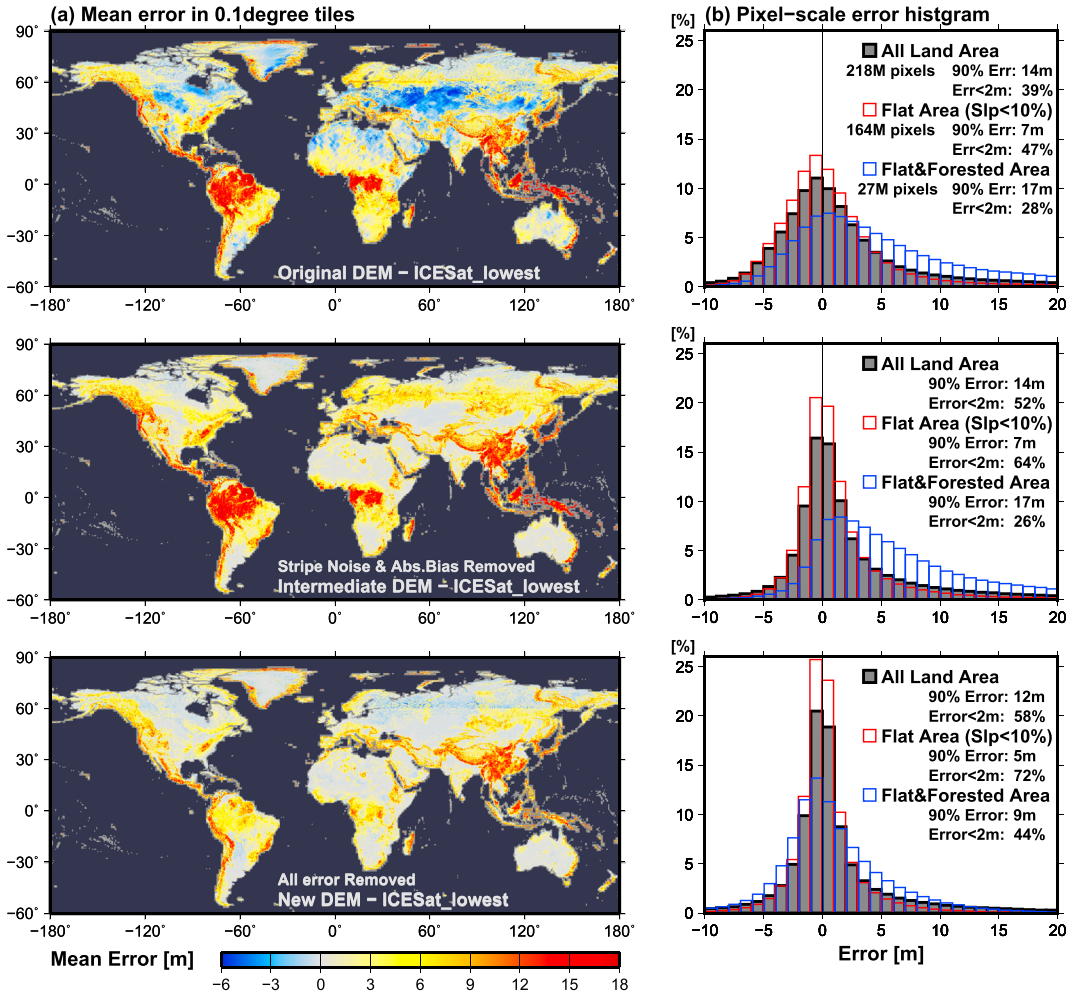

Figure 2. The difference between DEMs and ICESat lowest elevations. (a) Mean error in 0.1° tiles. (b) Pixel-scale error histogram for all land areas (gray), flat areas with topography slope <10% (red), and flat forested areas with tree density >30% (blue). The errors of the original DEM (top), the intermediate DEM after the removal of stripe noise and absolute bias (middle), and the new DEM after the removal of all error components (bottom) are shown. The number of ICESat measurements, the 90th percentile error and percentage of pixels with errors <2 m are summarized beside the error histograms.

the new DEM after error removal showed better agreement to the airborne lidar data. However, small absolute biases (<1 m) remained in areas away from the ICESat tracks. Furthermore, detailed topography, such as small river channels and levees, was not well represented in the new DEM compared to the local DEM due to the limited resolution of the former. This result suggests the importance of using more reference points for ground truth elevation and increasing the spatial resolution in order to further improve the accuracy of the global DEM.

4. Discussion

4.1. Landscape Analysis

The removal of the four error components from the original DEM largely improved the representation of landscape features (Figure 3). For example, previously the Sudd floodplain of the White Nile basin was significantly affected by stripe noise, and also parts of this area contain +10 m and −2 m absolute biases. Because of these errors, it is difficult to recognize the flow route of the White Nile River in the original DEM, but the main river channel and its floodplains are clearly represented in the new DEM. The transect profile (Figure 3a, fourth panel) also shows that the topography of the river channel and floodplains become more clearly separated

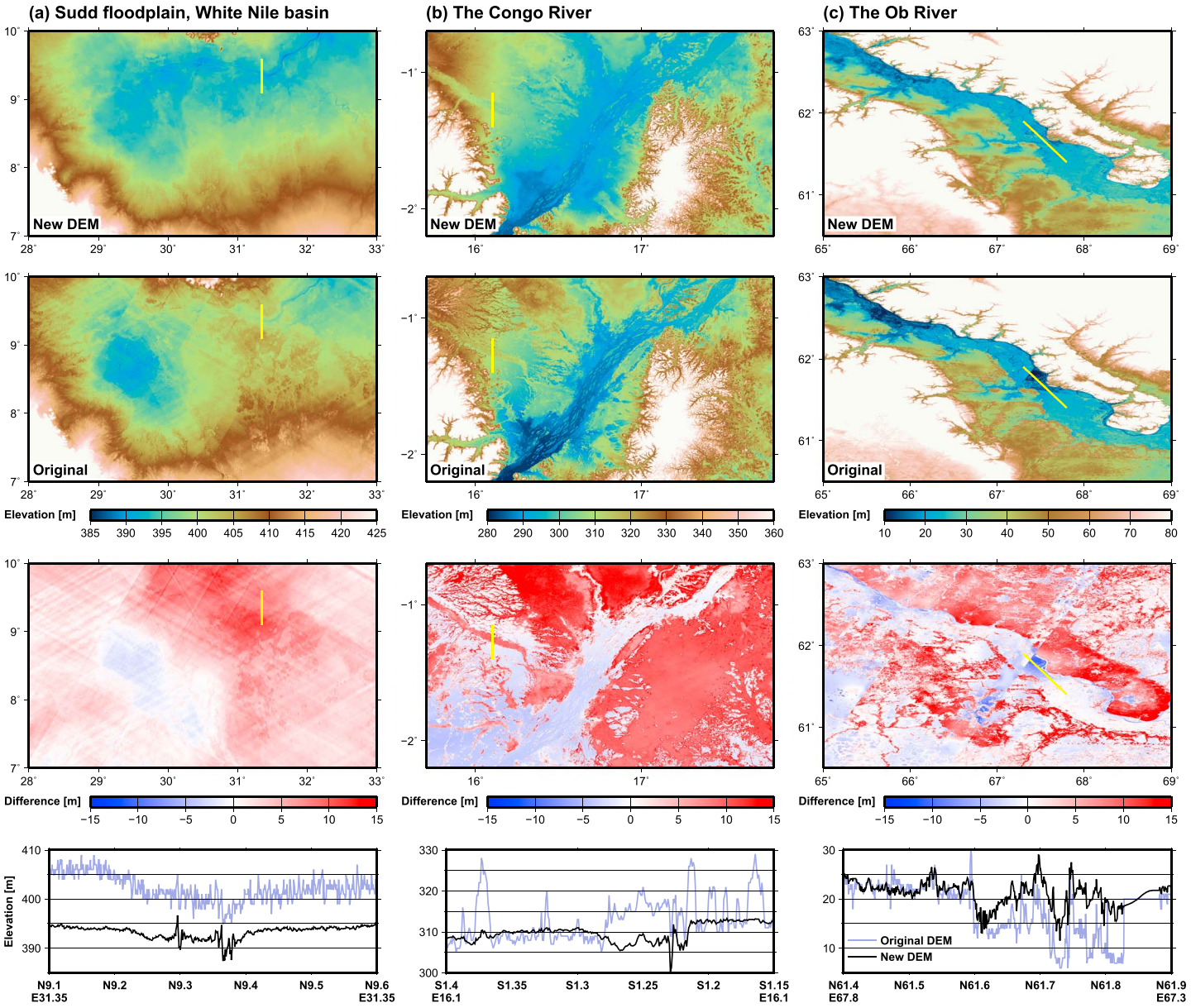

Figure 3. Closeup views of the modified terrain elevations, showing (from top to bottom) the new error-removed DEM, the original DEM, the removed height errors and the elevation profile of the yellow transect. Close up views of representative areas are shown for: (a) the Sudd floodplain of the White Nile basin, (b) the Congo River floodplain, and (c) the Ob River floodplain.

after removing stripe noise. In the Congo River floodplain, forest was dense in valleys such that elevations of these valleys were higher than the surrounding hills in the original DEM. These pseudo topographic reliefs were corrected by the error removal steps, and proper hill-valley structures are represented in the new DEM (Figure 3b). In the Ob River floodplain, spurious jumps in elevation values were observed due to absolute biases in the original AW3D DEM, while these discontinuities are reduced in the new DEM.

In order to detect regions where the true landscape relief had been significantly distorted by height errors at a global scale, we compared the actual topography slope and the pseudo slope caused by each error component. While the actual topography slope was calculated from the new DEM, the pseudo slope was given as the slope of each error component (for detailed definition, see supporting information Text S3 and Figure S10). The regions where topography slope was largely distorted by the height errors are highlighted in Figure 4. It was found that stripe and speckle noise affected the relief of many large river floodplains, such as the Parana, Niger, Nile, Indus, Ganges, Mekong, Murray-Darling, and Lake

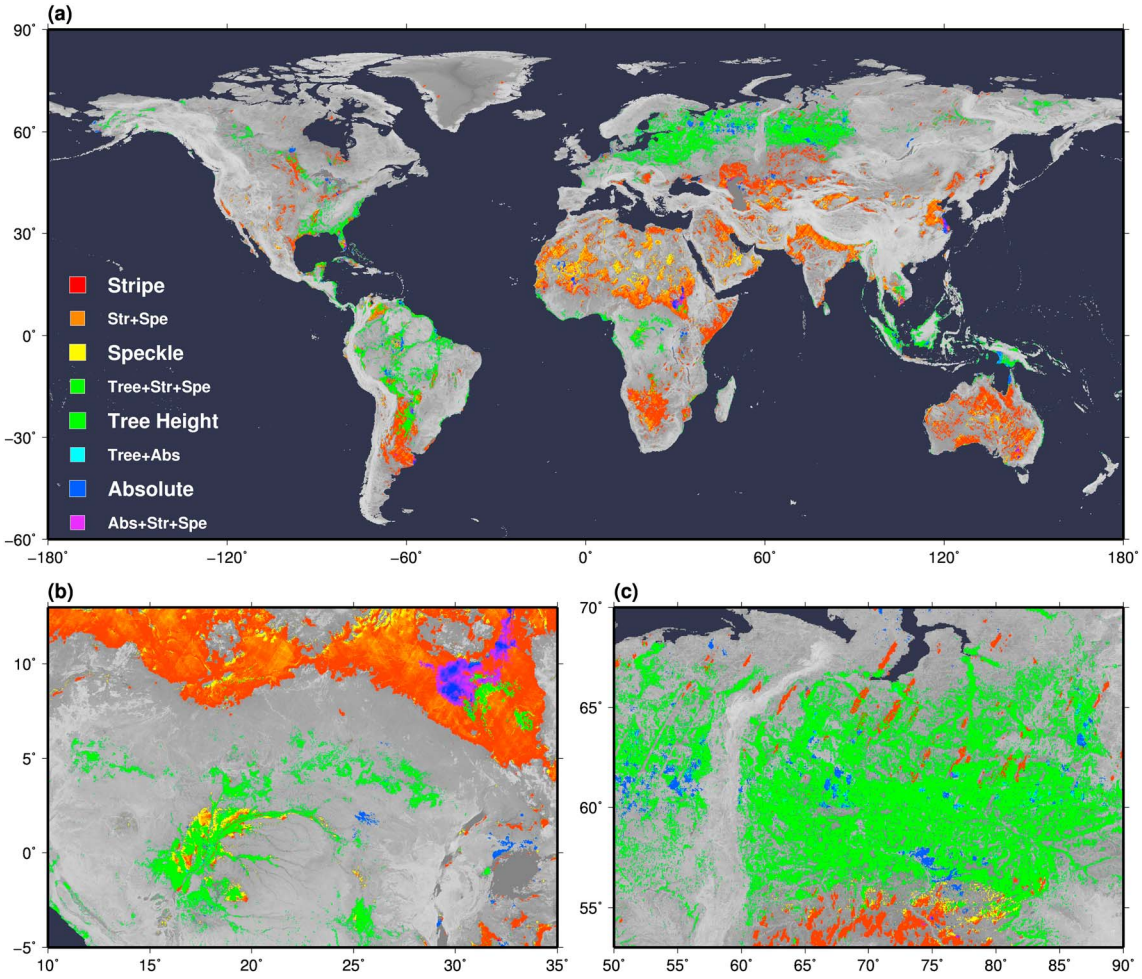

Figure 4. Regions significantly affected by height errors. The areas where the pseudo slope caused by each error component is larger than the actual topography slope are highlighted. Colors represent the error component causing terrain distortion. (a) Global view, (b) central area of the African continent, and (c) Western Siberia region. Background grayscale colors represent the topography slope.

Chad basins. Given that variability of topography relief is relatively small in these floodplains, errors in the elevation data could easily change the direction of terrain slopes and thus distort the representation of landscape features such as river drainage networks. Furthermore, absolute bias is usually not considered to affect topography slope because of its large spatial scale, but we found it actually distorted the slope in large floodplains of some continental-scale rivers, such as the Amazon, Niger, Nile, and Ob. These terrain distortions significantly degrade both geophysical simulations dependent on DEMs, such as flood inundation analysis, and subsequent applications of such analyses, such as calculation of biogeochemical fluxes.

Terrain slope distortion by tree height bias was observed only in flat regions where forested and nonforested areas have clear boundaries; however, the distorted locations could be critical for some important geoscience studies. Most of world's freshwater swamps, which are hotspots for wetland carbon dynamics [*Richey et al.*, 2002], were detected as regions significantly distorted by tree height bias. These areas include the central Amazonian floodplain, the Pantanal, the Congo swamp forest, the Vasyugan swamp in West Siberia, the Atchafalaya River in Louisiana, and Papua New Guinea's peat swamp. The topography of coastal areas with mangroves was also significantly affected by tree height bias, and this will degrade the estimation of water and carbon cycles in tidal and saline wetlands [*Chmura et al.*, 2003]. Given that flooding under vegetation canopies is difficult to detect by optical remote sensing [*Pekel et al.*, 2016], multisource approaches including precise DEM information [*Rudorff et al.*, 2014; *Fluet-Chouinard et al.*, 2015] are needed to estimate water and carbon dynamics in these wetlands. In addition, terrain distorted by

tree height bias was detected in the Eastern and Northern European Plains due to artificial deforestation [*Kaplan et al*., 2009] which creates further forest/nonforest boundaries in flat terrain.

4.2. Limitations and Future Plans

The quality of error-removed DEM highly depends on the original DEM sources. Including other DEM sources when available, such as the TanDEM-X DEM [*Krieger et al*., 2007] or NASADEM [*Crippen et al*., 2016], may in the future improve the quality of the global terrain elevation map. We limited the spatial resolution of the DEM analysis to 3″ mainly due to computational resource restrictions, but higher-resolution DEMs (e.g., 1″ resolution) have been made available in recent years [*Tadono et al*., 2015; *Dowling et al*., 2011; *Krieger et al*., 2007]. Our analysis suggests that the accuracy of the error-removed DEM is relatively low in mountainous areas where subpixel topography variability is large. Using higher-resolution DEMs will improve the quality of the terrain elevation mapping. Given that the algorithm developed in this study is mostly automated, applying the same method to newly available DEMs or higher resolution DEMs is not so difficult.

5. Conclusions

The new DEM developed in this study provides globally consistent terrain elevation data with a very high vertical accuracy. To date, terrain has been the "poor relation" when it comes to targets for global mapping and measurement campaigns [*Schumann et al*., 2014], yet such data are absolutely critical to numerous geoscience applications. Precise and accurate DEMs are needed by both satellite-data analysis [*Hough et al*., 2010; *Pekel et al*., 2016] and geophysical model studies [*Yamazaki et al*., 2014; *de Vente et al*., 2013], and DEM accuracy is likely to be important for integrating satellite observations into model simulations given that topography data are key to connecting conceptual models to reality [*Ward et al*., 2015]. The high-accuracy globally consistent mapping of terrain elevations achieved by this study will directly improve the representation of landscapes themselves and will further enable more clear-cut analysis and understanding of any of the many geophysical and biogeochemical processes which are terrain dependent. The newly constructed "Multi-Error-Removed Improved-Terrain DEM (MERIT DEM)" is freely available online for research and education purposes (http://hydro.iis.u-tokyo.ac.jp/~yamadai/MERIT_DEM/).

Acknowledgments
All baseline spaceborne DEMs and supplementary satellite data sets used for developing the new DEM are available online. The Multi-Error-Removed Improved-Terrain DEM (MERIT DEM) developed in this study is freely available for research and education purposes from the developer's webpage (http://hydro.iis.u-tokyo.ac.jp/~yamadai/MERIT_DEM/). This research was supported by "JSPS Grant-in-Aid for Scientific Research (16H06101 and 16H06291)." The authors would like to thank Junichi Takaku in RESTEC Japan for providing information on the known errors of in the AW3D DEM.

References

Baugh, C. A., P. D. Bates, G. J.-P. Schumann, and M. A. Trigg (2013), SRTM vegetation removal and hydrodynamic modeling accuracy, *Water Resour. Res.*, *49*, 5276–5289, doi:10.1002/wrcr.20412.

Berry, P. A. M., R. G. Smith, and J. Benveniste (2010), ACE2: The New Global Digital Elevation Model, *Gravity, Geoid and Earth Observation*, chap. 30, pp. 231–237, Springer, Berlin, doi:10.1007/978-3-642-10634-7_30.

Carabajal, C. C., and D. J. Harding (2006), SRTM C-band and ICESat laser altimetry elevation comparisons as a function of tree cover and relief, *Photogramm. Eng. Remote Sens.*, *72*, 287–298.

Chmura, G. L., S. C. Anisfeld, D. R. Cahoon, and J. C. Lynch (2003), Global carbon sequestration in tidal, saline wetland soils, *Global Biogeochem. Cycles*, *17*(4), 1111, doi:10.1029/2002GB001917.

Crippen, R., et al. (2016), NASADEM global elevation model: Methods and progress, ISPRS-International Archives of the Photogrammetry Remote Sensing and Spatial Information Sciences, *XLI-B4*, 125–128, doi:10.5194/isprs-archives-XLI-B4-125-2016.

Danielson, J. J., and D. B. Gesch (2011), Global multi-resolution terrain elevation data 2010 (GMTED2010), *U.S. Geol. Surv. Open File Rep., 2011–1073*, 26 p.

de Vente, J., J. Poesen, G. Verstraeten, G. Govers, M. Venmaercke, A. Van Rompaey, M. Arabkhedri, and C. Boix-Fayos (2013), Predicting soil erosion and sediment yield at regional scales: Where do we stand?, *Earth Sci. Rev.*, *127*, 16–27, doi:10.1016/j.earscirev.2013.08.014.

DiMiceli, C. M., M. L. Carroll, R. A. Sohlberg, C. Huang, M. C. Hansen, and J. R. G. Townshend (2011), *Annual Global Automated MODIS Vegetation Continuous Fields (MOD44B) at 250 m Spatial Resolution for Data Years Beginning Day 65, 2000–2010, Collection 5 Percent Tree Cover*, Univ. of Maryland, College Park. [Available at http://glcf.umd.edu/data/vcf/.]

Dowling, T. I., M. Brooks, and A. M. Read (2011), Continental hydrologic assessment using the 1 second (30 m) resolution Shuttle Radar Topographic Mission DEM of Australia, Proceeding of MSSANZ 2011 Perth, 2395–2401.

Farr, T. G., et al. (2007), The Shuttle Radar Topography Mission, *Rev. Geophys.*, *45*, RG2004, doi:10.1029/2005RG000183.

Fluet-Chouinard, E., B. Lehner, L. M. Rebelo, F. Papa, and S. K. Hamilton (2015), Development of a global inundation map at high spatial resolution from topographic downscaling of coarse-scale remote sensing data, *Remote Sens. Environ.*, *158*, 348–361, doi:10.1016/j.rse.2014.10.015.

Fricker, H. A., A. Borsa, B. Minster, C. Carabajal, K. Quinn, and B. Bills (2005), Assessment of ICESat performance at the salar de Uyuni, Bolivia, *Geophys. Res. Lett.*, *32*, L21S06, doi:10.1029/2005GL023423.

Gallant, J. (2011), Adaptive smoothing for noisy DEMs, *Proc. Geomorphometry*, *33*, 7–9.

Gallant, J., and A. Read (2009), Enhancing the SRTM data for Australia, *Proc. Geomorphometry*, *31*, 149–154.

Gesch, D. B., M. J. Oimoen, and G. A. Evans (2014), Accuracy assessment of the US Geological Survey National Elevation Dataset, and comparison with other large-area elevation datasets: SRTM and ASTER, *U.S. Geol. Surv. Open File Rep., 2014–1008*, 10, doi:10.3133/ofr20141008.

Hansen, M. C., et al. (2013), High-resolution global maps of 21st-century forest cover change, *Science*, *342*, 850–853, doi:10.1126/science.1244693.

Harding, D. J., and C. C. Carabajal (2005), ICESat waveform measurements of within-footprint topographic relief and vegetation vertical structure, *Geophys. Res. Lett.*, *32*, L21S10, doi:10.1029/2005GL023471.

Hirt, C., M. S. Filmer, and W. E. Featherstone (2010), Comparison and validation of the recent freely available ASTER-GDEM ver1, SRTM ver4.1 and GEODATA DEM-9S ver3 digital elevation models over Australia, *Aust. J. Earth Sci.*, *57*, 337–347, doi:10.1080/08120091003677553.

Hough, S. E., J. R. Altidor, D. Anglade, D. Given, M. G. Janvier, J. Z. Maharrey, M. Meremonte, B. S.-L. Mildor, C. Prepetit, and A. Yong (2010), Localized damage caused by topographic amplification during the 2010 M7.0 Haiti earthquake, *Nat. Geosci.*, *3*, 778–782, doi:10.1038/ngeo988.

Jarvis, A., H. I. Reuter, A. Nelson, and E. Guevara (2008), Hole-filled SRTM for the globe version 4, available from the CGIAR-CSI SRTM 90m Database. [Available at http://srtm.csi.cgiar.org.]

Johnson, B. D., and J. Singh (2003), Building the national geobase for Canada, *Photogramm. Eng. Remote Sens.*, *69*, 1169–1173, doi:10.14358/PERS.69.10.1169.

Kaplan, J. O., K. M. Krumhardt, and N. Zimmermann (2009), The prehistoric and preindustrial deforestation of Europe, *Quat. Sci. Rev.*, *28*, 3016–3034, doi:10.1016/j.quascirev.2009.09.028.

Krieger, G., A. Moreira, H. Fiedler, I. Hajnsek, M. Werner, M. Younis, and M. Zink (2007), TanDEM-X: A satellite formation for high-resolution SAR interferometry, *IEEE Trans. Geosci. Remote Sens.*, *45*, 3317–3341, doi:10.1109/TGRS.2007.900693.

Laudon, H., M. Berggren, A. Ågren, I. Buffam, K. Bishop, T. Grabs, M. Jansson, and S. Köhler (2011), Patterns and dynamics of dissolved organic carbon (DOC) in boreal streams: The role of processes, connectivity, and scaling, *Ecosystems*, *14*, 880–893, doi:10.1007/s10021-011-9452-8.

Martin, C. F., R. H. Thomas, W. B. Krabill, and S. S. Manizade (2005), ICESat range and mounting bias estimation over precisely-surveyed terrain, *Geophys. Res. Lett.*, *32*, L21S07, doi:10.1029/2005GL023800.

Maxwell, R. M., and L. E. Condon (2016), Connections between groundwater flow and transpiration partitioning, *Science*, *353*, 377–380, doi:10.1126/science.aaf7891.

O'Loughlin, F. E., R. C. D. Paiva, M. Durand, D. E. Alsdorf, and P. D. Bates (2016a), A multi-sensor approach towards a global vegetation corrected SRTM DEM product, *Remote Sens. Environ.*, *182*, 49–59, doi:10.1016/j.rse.2016.04.018.

O'Loughlin, F. E., J. Neal, D. Yamazaki, and P. D. Bates (2016b), ICESat-derived inland water surface spot heights, *Water Resour. Res.*, *52*, 3276–3284, doi:10.1002/2015WR018237.

Pekel, J.-F., A. Cottam, N. Gorelick, and A. S. Belward (2016), High-resolution mapping of global surface water and its long-term changes, *Nature*, *540*, 418–422, doi:10.1038/nature20584.

Richey, J. E., J. M. Melack, A. K. Aufdenkampe, V. M. Ballester, and L. L. Hess (2002), Outgassing from Amazonian rivers and wetlands as a large tropical source of atmospheric CO_2, *Nature*, *416*, 617–620, doi:10.1038/416617a.

Robinson, N., J. Regetz, and R. P. Guralnick (2014), EarthEnv-DEM90: A nearly-global, void-free, multi-scale smoothed, 90m digital elevation model from fused ASTER and SRTM data, *ISPRS J. Photogramm. Remote Sens.*, *87*, 57–67, doi:10.1016/j.isprsjprs.2013.11.002.

Rodriguez, E., C. S. Morris, and J. E. Belz (2006), A global assessment of the SRTM performance, *Photogramm. Eng. Remote Sens.*, *72*, 249–260, doi:10.14358/PERS.72.3.249.

Rudorff, C. M., J. M. Melack, and P. D. Bates (2014), Flooding dynamics on the lower Amazon floodplain: 1. Hydraulic controls on water elevation, inundation extent, and river-floodplain discharge, *Water Resour. Res.*, *50*, 619–634, doi:10.1002/2013WR014091.

Sampson, C. C., A. M. Smith, P. D. Bates, J. C. Neal, L. Alfieri, and J. E. Freer (2015), A high-resolution global flood hazard model, *Water Resour. Res.*, *51*, 7358–7381, doi:10.1002/2015WR016954.

Sampson, C. C., A. M. Smith, P. D. Bates, J. C. Neal, and M. A. Trigg (2016), Perspectives on open access high resolution digital elevation models to produce global flood hazard layers, *Front. Earth Sci.*, *3*, 1–6, doi:10.3389/feart.2015.00085.

Schumann, G. J.-P., P. D. Bates, J. C. Neal, and K. Andreadis (2014), Fight floods on a global scale, *Nature*, *507*, 169, doi:10.1038/507169e.

Simard, M., N. Pinto, J. Fisher, and A. Baccini (2011), Mapping forest canopy height globally with spaceborne lidar, *J. Geophys. Res.*, *116*, G04021, doi:10.1029/2011JG001708.

Tachikawa, T., M. Hato, M. Kaku, and A. Iwasaki (2011), Characteristics of ASTER GDEM version 2, Proceeding of 2011 IEEE International Geoscience and Remote Sensing Symposium (IGARSS), 3657–3660, doi:10.1109/IGARSS.2011.6050017.

Tadono, T., J. Takaku, K. Tsutsui, F. Oda, and H. Nagai (2015), Status of "ALOS World 3D (AW3D)" global DSM generation, Proceeding 2015 IEEE International Geoscience and Remote Sensing Symposium (IGARSS), 3822–3825, doi:10.1109/IGARSS.2015.7326657.

Takaku, J., T. Tadono, K. Tsutsui, and M. Ichikawa (2015), Quality status of high resolution global DSM generated from ALOS PRISM, Proceeding of 2015 IEEE International Geoscience and Remote Sensing Symposium (IGARSS), 3854–3857, doi:10.1109/IGARSS.2015.7326665.

Takaku, J., A. Iwasaki, and T. Tadono (2016), Adaptive filter for improving quality of ALOS PRISM DSM, Proceeding of IEEE Geoscience and Remote Sensing Symposium (IGARSS) 2016, 5370–5373, doi:10.1109/IGARSS.2016.7730399.

Tang, L., V. V. Titov, and C. D. Chamberlin (2009), Development, testing, and applications of site-specific tsunami inundation models for real-time forecasting, *J. Geophys. Res.*, *114*, C12025, doi:10.1061/(ASCE)WW.1943-5460.0000357.

Tarekegn, T. H., and T. Sayama (2013), Correction of SRTM DEM artefacts by Fourier transform for flood inundation modeling, *J. Jpn Soc. Civ. Eng. B1*, *69*, 193–198.

Ward, P. J., et al. (2015), Usefulness and limitations of global flood risk models, *Nat. Clim. Change*, *5*, 712–715, doi:10.1038/nclimate2742.

Yamazaki, D., T. Sato, S. Kanae, Y. Hirabayashi, and P. D. Bates (2014), Regional flood dynamics in a bifurcating mega delta simulated in a global river model, *Geophys. Res. Lett.*, *41*, 3127–3135, doi:10.1002/2014GL059744.

Yamazaki, D., M. A. Trigg, and D. Ikeshima (2015), Development of a global ~90 m water body map using multi-temporal Landsat images, *Remote Sens. Environ.*, *171*, 337–351, doi:10.1016/j.rse.2015.10.014.